Direct comparison of EUV and visible-light interferometries

Kenneth A. Goldberg[*a], Patrick Naulleau[a], SangHun Lee[a,b], Chang Chang[a,b], Cynthia Bresloff[c],
Richard Gaughan[d], Henry N. Chapman[d], John Goldsmith[e], and Jeffrey Bokor[a,b]

[a]Center for X-Ray Optics, Lawrence Berkeley National Laboratory, Berkeley, CA 94720
[b]EECS Department, University of California, Berkeley, CA 94720
[c]Steward Observatory, University of Arizona, Tuscon, AZ 85721
[d]Lawrence Livermore National Laboratory, L-395, Livermore, CA 94550
[e]Sandia National Laboratories, PO Box 969, MS 9409, Livermore, CA 94551

ABSTRACT

Recent experiments with four 10× EUV imaging systems provide the first direct comparisons of visible-light and at-wavelength EUV interferometries performed using the state-of-the-art measurement tools that will be used to assemble and align the next generation of EUV imaging systems. Measurements from four individual multilayer-coated Schwarzschild objectives are discussed. Favorable agreement has been achieved between EUV and visible-light system wavefront measurements in all four optical systems. Measurements made in the presence of surface contamination and multilayer thickness variation, however, do show expected localized differences between the two measurements.

Keywords: interferometry, extreme ultraviolet lithography, EUV, surface figure measurement, point-diffraction interferometer, at-wavelength testing, Schwarzschild objective

1. INTRODUCTION

Interferometry is an optical technique by which an optical system can be measured and thereby improved. Wavefront interferometry is also routinely used to predict lithographic imaging performance. Due to the extremely stringent fabrication and alignment tolerances for EUV lithographic optical systems, considerable attention has been paid in recent years to the development of high-accuracy metrology tools compatible with EUV optics.

Several different EUV interferometers have been developed over the past decade. Foucault [1] and Ronchi [2] testing for alignment of EUV optics have been demonstrated using both synchrotron [3] and laser-plasma [4] light sources. Other significant research includes refinement of the lateral shearing interferometer [5], and the point diffraction interferometer (PDI) [6, 7, 8].

The most successful of the EUV interferometers to date has been the recently-developed phase-shifting point diffraction interferometer (PS/PDI), first proposed by Medecki [9, 10]. While the PS/PDI preserves the advantages of the PDI, using pinhole diffraction to generate a spherical reference wavefront in the image plane, it represents a significant step forward. With substantially higher efficiency and the introduction of phase-shifting capability, the PS/PDI has become one of the most accurate system-level measurement tools of its kind. Its reference wavefront accuracy has been demonstrated as high as 0.04 nm rms in a numerical aperture of 0.08, well beyond the present requirements for EUV optical system metrology.

Advanced visible-light [11, 12, 13] and EUV interferometric techniques possessing the required measurement accuracy are being developed. Visible-light has clear advantages in optical shop testing where it can be used to measure single, un-coated elements. Yet, the EUV wavefront is determined both by the geometric figure of the mirror surfaces and by the properties of the multilayer coatings, which are deposited across mirror areas covering many square inches. It is for this reason, that at-wavelength EUV testing is the most direct probe of the sensitive resonance properties of reflective multilayer coatings. Coating thickness gradients, designed to achieve optimal reflectivity in the presence of a range of incidence angles, and surface contamination can both cause differences between visible-light and EUV wavefront measurements.

We present EUV and visible-light measurements of four individual 10× Schwarzschild objective imaging systems, or *cameras*. These optics have been essential to the development of EUV lithographic technology in recent years, and they

---

[*]Correspondence: Email: KAGoldberg@lbl.gov; Telephone: 510-495-2261; Fax: 510-486-4550

provide the first opportunity for comparison of the two measurement techniques. The cameras were measured using the diffraction-based visible and EUV interferometers being developed by the Virtual National Laboratory (VNL) for the EUV LLC. These tools are the EUV PS/PDI [14] which operates at the Advanced Light Source (ALS) at Lawrence Berkeley National Laboratory (LBNL), and the Sommargren phase-shifting diffraction interferometer (PSDI) [11] implemented at Lawrence Livermore National Laboratory LLNL. Detailed descriptions of both of these interferometers are available in the literature.

The reflection of EUV and visible-light from the multilayer coatings can be described in different ways. While visible-light probes the surface position, the resonant EUV reflection depends sensitively on wavelength, incident-angle, and local layer thickness. Yet even in the presence of spatially graded coatings, optical modeling of the 10× camera system performed with CodeV shows that the visible and EUV wavefronts differ in principle by only a few thousandths of an EUV wavelength, or a few tenths of an angstrom. [15].

The design goal for the alignment of EUV lithographic systems with 0.1 NA calls for aberrations magnitudes below 0.26 nm rms (λ/50 at 13.4 nm). To maintain confidence in the alignment and characterization procedures, the EUV and visible-light interferometries must have precision *and accuracy* superior to this level. This suggests that the agreement between visible-light and EUV interferometries needs to be within one-hundredth of an EUV wavelength, or 0.13 nm.

Recently, the spherical reference wavefront quality of the EUV PS/PDI interferometer has been measured to be 0.04 nm rms within 0.08 NA [16]. However, the inherent reference wavefront accuracy of an interferometer does not guarantee an accurate measurement. Knowledge of the measured conjugate position, relative to the optical system under test, plays an essential role in system alignment. Likewise, the quality of the comparison depends on a the use of a shared conjugate point coordinate system. This paper presents the status of the comparisons to date, and describes limitations present in the available data which give rise to systematic uncertainties.

2. FOUR 10× SCHWARZSCHILD CAMERAS

We present the comparison of four separate 10× Schwarzschild cameras fabricated to the same optical design specifications, and built during the last five years. The numerical apertures (NA) of the cameras used for the comparison of the two interferometry methods ranges from 0.08 to 0.088. These optics utilize molybdenum/silicon multilayer coatings with 40 bi-layer pairs, designed for peak reflectivity near 13.4 nm wavelength. The cameras are described as follows.

10×B: (*fabricated in 1994*) Used in the development of EUV interferometry, and in EUV imaging at Sandia National Laboratories (SNL). [17] Coated at AT&T.

10×I: (*fabricated 1993-4*) The original 10×I microstepper optic used at SNL [18]. Coated at AT&T.

Camera 3: (*fabricated in 1997-8*) A recently-built camera developed to meet the figure specifications of the Projection Optics Box (POB) [19]. Coated at LLNL [20].

Camera 1: (*fabricated in 1998*) A recently-built camera developed to meet the figure *and finish* specifications of the Projection Optics Box (POB) [21]. Coated at LLNL.

Of the four cameras, 10×B and 10×I were first measured at-wavelength, and were subsequently measured with visible-light, while Camera 3 and Camera 1 were both measured during visible-light alignment, prior to EUV testing.

3. UNCERTAINTY IN THE WAVEFRONT MEASUREMENT

Between the visible-light and the EUV wavefront measurements, there exists a systematic uncertainty related to the positions of the conjugate points used in the two interferometers. Both systems have the freedom to measure the optic over a range of conjugate field points. On the object (mask) side, this range extends several millimeters laterally and longitudinally. The 10× camera is designed for a field of view that is 400-µm-diameter in the image plane (wafer side), and consequently is 4-mm-diameter in the object (mask) plane.

Uncertainty in the conjugate positions translates into systematic uncertainties in the measured wavefronts, and hence in the comparison as well. Analysis of the optical design shows that longitudinal and lateral adjustment of the object-point position both introduce astigmatism into this off-axis system. Coma is also introduced by

Table 1. Sensitivity to object displacement from the nominal position. Zernike coefficient magnitudes (and wavefront rms) values are shown.

per 1.0 mm displacement	astigmatism [nm]	coma [nm]
x	0.339 (0.138)	0.015 (0.005)
y	0.165 (0.068)	0.212 (0.075)
z	0.816 (0.332)	0.240 (0.084)

lateral object translation in the direction of the off-axis sub-aperture. Table 1 contains the sensitivities (wavefront aberration per object translation) calculated using a *CodeV* model of the 10× camera design. To calculate the sensitivities, a full description of the optical system was used, including the measured multilayer coating thickness profiles of both elements. Shown are the effects of 1 mm displacement of the object position along three orthogonal axes. z is the longitudinal axis, and y is the lateral axis in the direction of the off-axis sub-aperture.

Because Cameras 1 and 3 were both aligned using visible-light interferometry, the two mirror elements were positioned to achieve the minimum wavefront rms at a chosen object field point [22]. A kinematic alignment fixture was designed to make identification of the object position, and hence the wavefront measurement, repeatable. When the cameras were brought to LBNL for EUV measurement, where a comparable alignment tool was unavailable, a systematic search of the field-of-view was performed to identify both the position of minimum rms wavefront errors and the position of best EUV/visible-light wavefront agreement. Even though the optics were aligned for the optimal wavefront rms, in both cases there was some residual astigmatism present. To address the conjugate position uncertainty (and with it, the associated astigmatism uncertainty), the comparisons are made at the conjugate position of best agreement.

The older cameras, 10×I and 10×B were originally aligned using visible-light interferometry that predates the PSDI. These cameras were tested in the PSDI following measurement at-wavelength, The conjugate position uncertainty also affects the comparisons of these two optics.

4. WAVEFRONT COMPARISON

The comparisons of EUV and visible-light wavefront measurements performed on all four cameras reveals good agreement between these two very different measurement tools. The comparison procedure is the same for all of the optics. The pairs of wavefronts (EUV and visible-light) are carefully studied to create a shared coordinate system and identify the region of valid comparison data. All of the optics are designed for peak reflectivity at 13.4 nm. EUV measurements shown here were all made at that wavelength.

The EUV and visible wavefront data sets come from different detectors with different orientations and scaling on their respective pixel arrays. Alignment of the data sets is performed by hand, using the wavefronts themselves to guide the selection of the shared coordinate system: one wavefront must be rotated and scaled into position, overlapping the other. For this purpose, the smallest observable wavefront features serve well as ad hoc fiducial reference marks identifiable in both EUV and visible wavefronts.

The subregion of the data sets that is used in the comparison is usually narrower than the full width of the available data by more than one percent. The circular aperture stop rests close to the surface of the primary and functions as an entrance pupil for the camera. It casts a shadow that contains a bright, narrow diffraction ring around the edge of the visible-light data set. The points near the edge of the visible-light measurement domain show a sharp phase slope and are therefore not included in the comparison. In addition, the back side of the primary mirror substrate obscures a small set of rays closest to mechanical axis of the system, and also produces a diffraction edge that must be excluded.

Once a shared coordinate system and valid data region have been established, a unique basis set of orthogonal aberration polynomials must be determined. Aberration polynomials are based on the familiar Zernike Circle polynomials using a process of Gram-Schmidt orthogonalization [23] to guarantee orthogonality over the common data region. Each comparison requires its own set of orthogonal polynomials. The measurement-dependent *piston*, *tilt*, and *defocus* terms are always subtracted from the data to facilitate comparison.
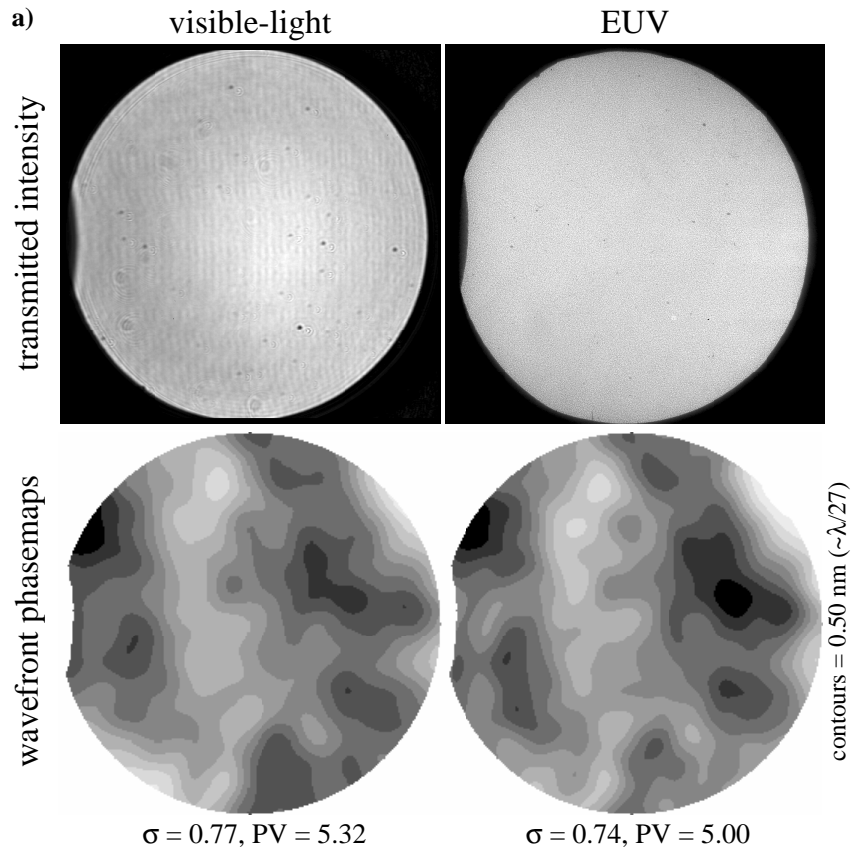
Although low and mid-spatial-frequency information is preserved in the wavefront phasemaps of both interferometers, the comparisons and wavefront statistics presented in this article are all based on 37-term orthogonal polynomial fitting.
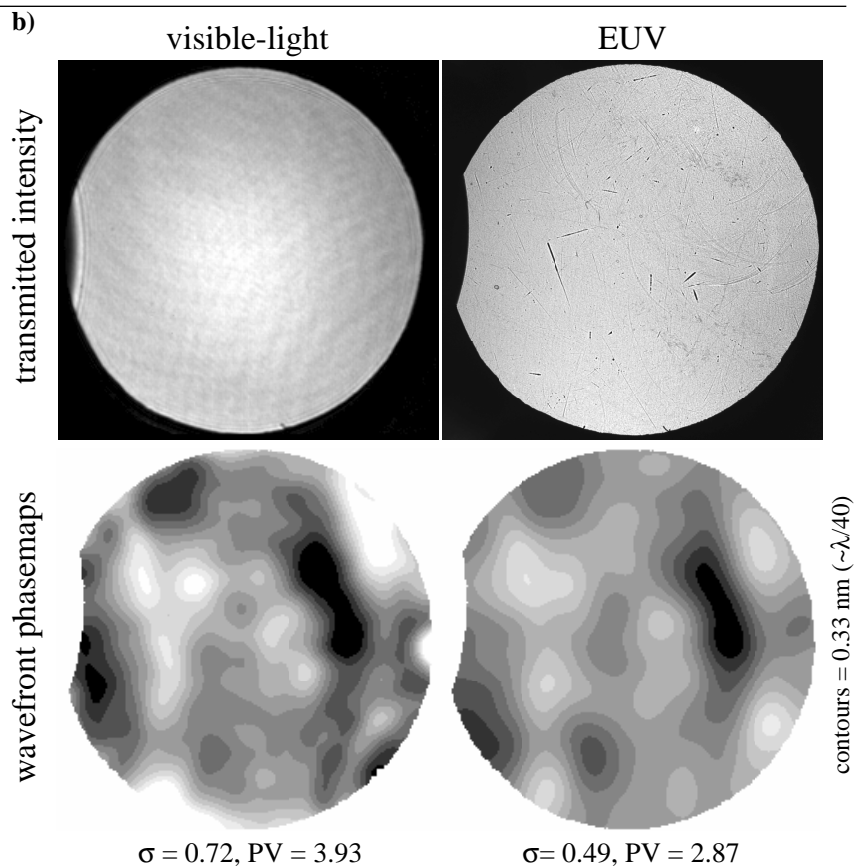
4.1. Camera 1 and Camera 3

Cameras 1 and 3 are two of the recently fabricated Schwarzschild objectives, and they possess the highest-quality wavefront figure of the four cameras compared here. Both optics are virtually free of observable surface contamination or blemishes of the type seen in the previous generation of 10× cameras. Figure 1a shows the comparison of Camera 1 data, while Fig. 1b shows the comparison of Camera 3. Statistics for the comparisons are shown in Table 2, and a comparison of the Zernike polynomial fit coefficients are shown in Fig. 2.

Figure 1. Camera 3 (a) and Camera 1 (b) transmitted intensity and wavefront comparison. Wavefront statistics are based on a 37-term Zernike polynomial fit. The numerical apertures used in the wavefront comparisons are 0.083 for Camera 3 and 0.087 for Camera 1. The EUV and visible-light wavefront phasemap data are rotated, scaled, and aligned to match; the transmitted intensity images are not.

Camera 3

Camera 1

a)

visible-light   EUV

transmitted intensity

wavefront phasemaps

contours = 0.50 nm (~λ/27)

σ = 0.77, PV = 5.32   σ = 0.74, PV = 5.00

b)

visible-light   EUV

transmitted intensity

wavefront phasemaps

contours = 0.33 nm (~λ/40)

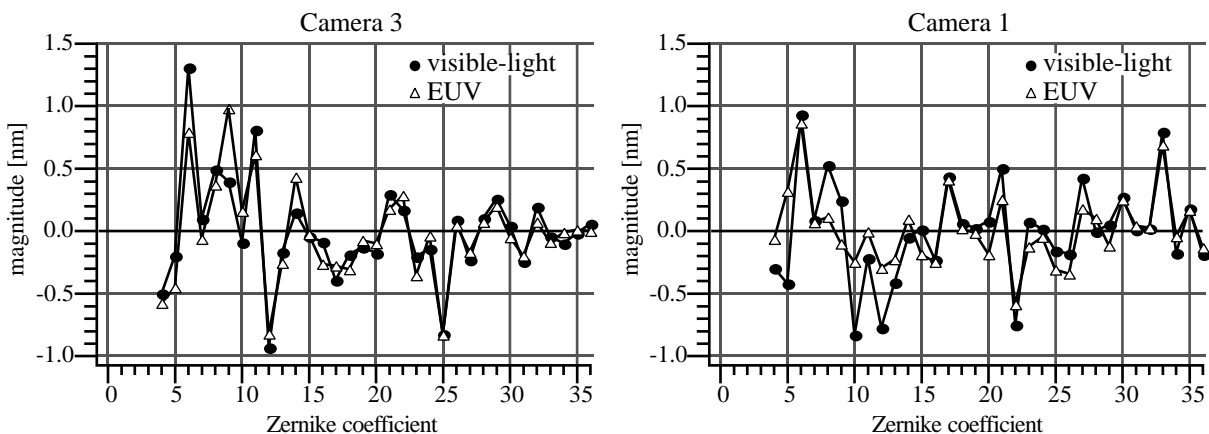σ = 0.72, PV = 3.93   σ= 0.49, PV = 2.87

Figure 2. Comparison of Zernike polynomial fit coefficients for the EUV and visible-light wavefronts shown in Fig. 1.

Table 2. Wavefront comparisons of Cameras 3 and 1. The rms (σ) and peak-to-valley (PV) magnitudes are shown for the visible light wavefront Φ_{vis}, the EUV wavefront Φ_{EUV}, and the *difference wavefront* , $\Delta\Phi$, defined as $\Phi_{vis} - \Phi_{EUV}$. Due to the unknown conjugate positions between the two measurements, astigmatism is responsible for the most significant discrepancy and the greatest uncertainty. To gauge the importance of the unknown astigmatism, comparison statistics are also presented for wavefronts with the astigmatism removed entirely.

Camera 3, 0.083 NA

	σ, PV [nm]	astig. removed σ, PV [nm]
Φ_{vis}	0.77, 5.32	0.74, 4.90
Φ_{EUV}	0.74, 5.00	0.68, 4.17
$\Delta\Phi$	0.36, 2.27	0.34, 1.87

Camera 1, 0.087 NA

	σ, PV [nm]	astig. removed σ, PV [nm]
Φ_{vis}	0.72, 3.93	0.69, 3.49
Φ_{EUV}	0.49, 2.87	0.48, 3.49
$\Delta\Phi$	0.49, 3.66	0.38, 2.50

In addition to the wavefront comparisons, the transmitted intensity of visible and EUV light are also shown in the figures. The visible-light transmitted intensity is recorded as a part of the wavefront measurement. The similar EUV measurement is recorded prior to interferometry, during the interferometer's alignment procedure.

During EUV and visible measurements, the aperture stop in Camera 3 became displaced from its resting position close to the downward-facing primary mirror's surface. When the circular aperture drops down, it obstructs some of the rays farthest from the mechanical axis of the system, creating an elliptical pupil. For this reason, a smaller NA was available for the wavefront comparison than for Camera 1.

While the wavefront of Camera 1 is superior to that of Camera 3, the quality of the comparisons are comparable, based on the rms of the difference wavefront. However, the NA under consideration in the Camera 1 comparison is more than 4% larger. Since aberration magnitudes typically scale with powers of the NA (i.e. astigmatism scales with r^2, coma with r^3, etc.), the Camera 1 comparison over 0.087 NA is a more stringent test.

4.2. 10×I and 10×B Cameras

Although the two older cameras have each played important roles in the development of EUV lithographic technology during the past few years, these optics are of significantly lower quality than Cameras 1 and 3 in many ways.

EUV transmitted intensity images reveal numerous small defects in both cameras. The appearance of 10×I (Fig. 3) is dominated by a single 1-mm-scale blemish, within which the EUV reflectivity is reduced. Also present are a number of long scratches which may be the by-product of the polishing technique used in the preparation of the substrates. 10×B contains numerous small, 100-µm-scale defects, which have the appearance of streaks, residue left by a wet cleaning process. The circular, 0.08 NA aperture stop of 10×B was broken, leaving a D-shaped pupil. The only available transmitted intensity image from this, the best sub-aperture of 10×B [24], shows the pupil spatially filtered by transmission through a 4.5-µm square window in the image plane. While only some of the defects appear in the visible-light transmitted intensity images, all of them appear in the visible-light wavefront.
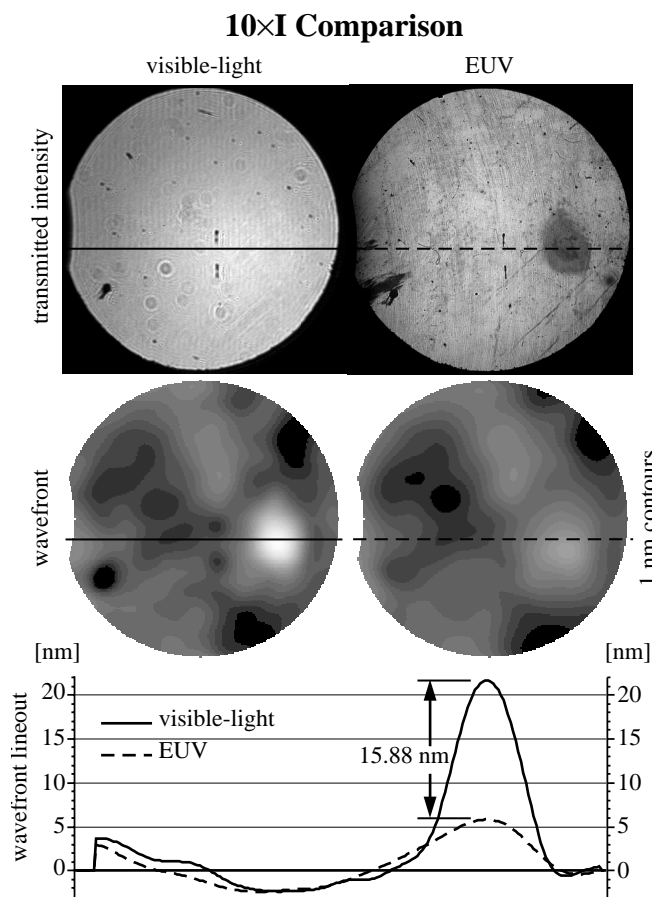
10×I Comparison

visible-light   EUV

Figure 3. Visible-light and EUV comparison of the transmitted intensity and wavefront phase in the 10×I camera within an NA of 0.08. Wavefront agreement is very good overall, except in the region of the blemish where the EUV and visible-light response is different. The solid and dashed cross-section lines indicate the position of the wavefront line-out shown in the graph.

10×B Comparison

visible-light   EUV

Figure 4. Visible-light and EUV comparison of the transmitted intensity and wavefront phase in the 10×B camera. The EUV intensity data is spatially filtered by a 5-µm-square window in the image-plane. Numerous small defects where data is not available are masked from the EUV wavefront phasemap. These defects appear as small bumps in the visible-light wavefront, on the order of 1 nm. While agreement is very good over the circular 0.08 NA sub-aperture the optic was designed to use, at the edge of the D-shaped aperture, where the coating thickness decreases, the two wavefronts diverge. The solid and dashed lines indicate the positions of the wavefront lineouts in the graph. The surface height change is partially compensated by an EUV phase change, as predicted.

4.2.1. 10×I

The EUV and visible-light wavefronts of 10×I compare very well, except in the region of the blemish. Within the blemish, the visible-light and EUV wavefronts differ by nearly 16 nm (1.2 λ). In order to make a successful comparison under these circumstances, the Zernike polynomial fitting was performed on a domain that excludes the blemish region. The appropriate amounts of piston, tilt, and defocus could then be removed from the wavefronts over the full domain. Figure 3 shows a comparison of the wavefront phasemaps, and a lineout, or cross-section, of the wavefront surface data made through the blemish.

The data demonstrate the way in which surface contamination can respond differently to EUV and visible-light. While the blemish is unobserved in the visible intensity image, its presence is very pronounced in the wavefront. Surface contamination thus creates the potential for misinterpretation of the wavefront data when EUV measurements are not made.
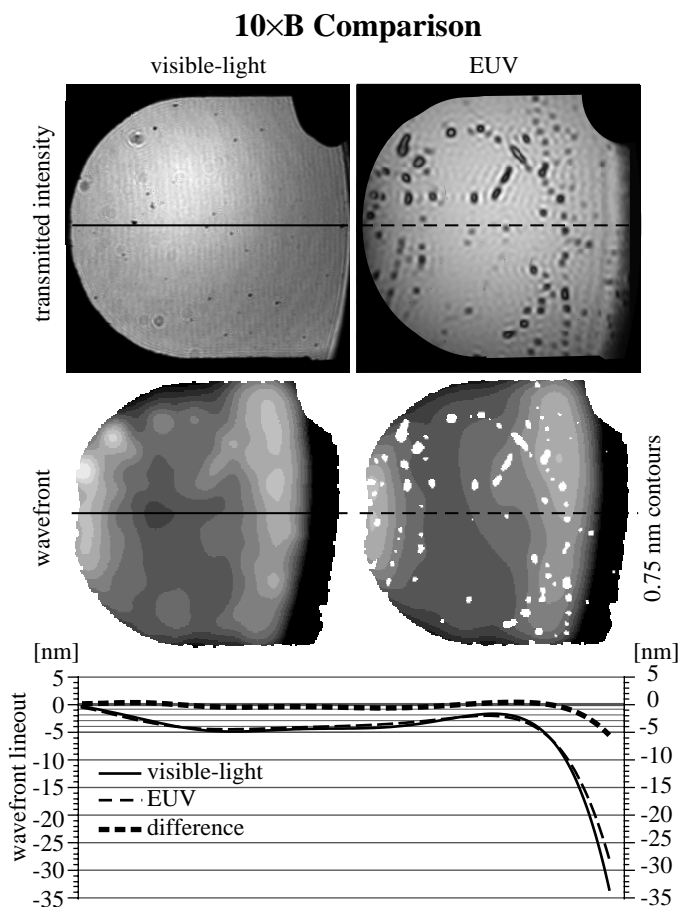
6

4.2.2. 10×B

The wavefront agreement observed in 10×B is also very good overall; however,10×B reveals a different kind of discrepancy, related to changes in the multilayer coating thickness, or *d*-spacing. This optic was originally designed to be used with NA values below 0.08. The coating properties change abruptly near the edge of the mirrors where the control of the coating parameters was not important to the design. The D-shaped aperture reveals the outer edges of the mirrors, and enables the comparison to extend into the region where the coating thickness decreases rapidly over a short distance. The wavefront comparison for this camera is shown in Fig. 4.

Because no EUV wavefront data is available within the dark defect regions, these areas were masked from the wavefront surface fitting of both the EUV and the visible-light data. The small defects appear as bumps in the visible-light wavefront, approximately 1 nm high.

Near the edge of the domain, the wavefront slope changes abruptly. Both the EUV and visible-light wavefronts follow the changing surface height, but the two measurements diverge by more than 5 nm.

It is easily shown for multilayer reflection near normal incidence, that the geometric path-length change that accompanies a change in the layer thickness relative to a fixed substrate position is partially compensated by a phase-change upon reflection. For this particular system with 40 bi-layer pairs, the phase-change, separate from the geometric path-length change, is predicted to be approximately one wave per 7.5 $\Delta d/d$ [25], or, equivalently, 100 nm per fractional change in layer thickness, $\Delta d/d$. From reflection, we assume the total coating thickness change to be equal to one-half of the observed visible-light wavefront height change, or about 17 nm. With a total coating thickness of $(40 \times 13.4 \text{ nm} \div 2 =)$ 268 nm, the fractional change is 6.3%, and the predicted EUV phase shift is $(100 \times 0.063 =)$ 6.3 nm. The observed difference is 5.6 nm, within 11% of the expected value.

5. CONCLUSION

Recent EUV and visible-light interferometric cross-correlation experiments, performed with four different 10× EUV cameras have shown very good agreement over numerical apertures beyond 0.08. Wavefront differences on the order of a few tenths of a nanometer fall within a measurement uncertainty level set by the unknown conjugate positions between the two measurements. The wavefront measurements are observed to diverge, as expected, in the presence of surface contamination and rapid coating thickness variation.

6. ACKNOWLEDGEMENTS

7. REFERENCES

1. L. M. Foucault, "Description des procedees employes pour reconnaitre la configuration des surfaces optiques," C. R. Acad. Sci. (Paris), **47**, 958, 1858.

2. V. Ronchi, "Due Nuovi Metodi per lo Studio delle Superficie e die Sistemi Ottici," Ann. Sc. Norm. Super. Pisa, **15**, 1923.

3. E. Tejnil, K. A. Goldberg, S. H. Lee, H. Medecki, *et al.,* "At-wavelength interferometry for EUV lithography," Journal of Vacuum Science & Technology B **15** (6), 2455-2461, 1997.

4. A. K. Ray-Chaudhuri, K. D. Krenz, R. P. Nissen, *et al.*, "Initial results from an extreme ultraviolet interferometer operating with a compact laser plasma source," Journal of Vacuum Science & Technology B **14** (6), 3964-8, 1996.

5. J. E. Bjorkholm, A. A. MacDowell, O. R. Wood II, Z. Tan, *et al.*, "Phase-measuring interferometry using extreme ultraviolet radiation," Journal of Vacuum Science & Technology B **13** (6), 2919-22, 1995.

6. K. A. Goldberg, R. Beguiristain, J. Bokor, H. Medecki, K. Jackson, and D. T. Attwood, "Point Diffraction Interferometry at EUV Wavelengths," OSA Proceedings on Extreme Ultraviolet Lithography, Vol. **23**, F. Zernike and D. T. Attwood (eds.), 134-141, 1994.

7. K. A. Goldberg, R. Beguiristain, J. Bokor, H. Medecki, K. Jackson, and D. T. Attwood, G. E. Sommargren, J. P. Spallas, and R. Hostetler, "At-wavelength testing of optics for EUV," Proc. SPIE **2437**, 347-54, 1995.

8. K. A. Goldberg, R. Beguiristain, J. Bokor, H. Medecki, D. T. Attwood, K. Jackson, E. Tejnil, and G. E. Sommargren, "Progress toward λ/20 EUV interferometry," Journal of Vacuum Science & Technology B **13** (6), 2923-7, 1995.

9. H. Medecki, E. Tejnil, K. A. Goldberg, and J. Bokor, "Phase-shifting point diffraction interferometer," Optics Letters **21** (19), 1526-28, 1996.

10. H. Medecki, U.S. Patent 5,835,217: "Phase-shifting point diffraction interferometer," Nov. 1998.

11. G. E. Sommargren, "Phase shifting diffraction interferometry for measuring extreme ultraviolet optics," in OSA Trends in Optics and Photonics, Vol. 4, Extreme Ultraviolet Lithography, G. D. Kubiak and D. R. Kania, Eds., Optical Society of America, Washington, D.C., 108-12, 1996.

12. G. E. Sommargren, "Diffraction methods raise interferometer accuracy," Laser Focus World **32** (8), 61-71, 1996.

13. G. E. Sommargren, U.S. Patent 5,548,403: "Phase shifting diffraction interferometer," Aug. 1996.

14. K. A. Goldberg, E. Tejnil, S. H. Lee, H. Medecki, D. T. Attwood, K. H. Jackson, and J. Bokor, "Characterization of an EUV Schwarzschild objective using phase-shifting point diffraction interferometry," Proc. SPIE **3048**, 264-70, 1997.

15. C. Bresloff, *personal communication.*

16. P. Naulleau, K. A. Goldberg, S. Lee, C. Chang, C. Bresloff, P. Batson, D. Attwood, and J. Bokor, "Characterization of the accuracy of EUV phase-shifting point diffraction interferometry," in Emerging Lithographic Technologies II, Y. Vladimirski, ed., Proc. SPIE **3331**, 114-23, 1998.

17. K. A. Goldberg, P. Naulleau, S. Lee, C. Bresloff, C. Henderson, D. Attwood, and J. Bokor, "High-accuracy interferometry of EUV lithographic optical systems," Journal of Vacuum Science and Technology B **16** (6), 3435-3439, 1998.

18. D. A. Tichenor, A. K. Ray-Chaudhuri, G. D. Kubiak, *et al.*, "Development and characterization of a 10x Schwarzschild system for SXPL," in OSA Proceedings on Soft X-Ray Projection Lithography, Vol. 18, A. M. Hawryluk and R. H. Stulen, eds., Optical Society of America, Washington, D.C., 79-82, 1993.

19. D. W. Sweeney, R. Hudyma, H. N. Chapman, and D. Shafer, "EUV optical design for a 100 nm CD imaging system," in Emerging Lithographic Technologies II, Y. Vladimirski, ed., Proc. SPIE **3331**, 2-10, 1998.

20. E. A. Spiller, F. J. Weber, C. Montcalm, S. L. Baker, E. M. Gullikson, J. H. Underwood, "Multilayer coating and tests of a 10X extreme ultraviolet lithographic camera," in Emerging Lithographic Technologies II, Y. Vladimirski, ed., Proc. SPIE **3331**, 62-71, 1998.

21. J. E. M. Goldsmith, K. W. Berger, D. R. Bozman, G. F. Cardinale, *et al.*, "Sub-100-nm imaging with the EUV 10x Microstepper," in Emerging Lithographic Technologies III, Y. Vladimirski, ed., Proc. SPIE **3676**, this volume, 1999.

22. H. N. Chapman and D. W. Sweeney, "A rigorous method for compensation selection and alignment of microlithographic optical systems," Proc. SPIE **3331**, 102-113, 1998.

23. D. J. Fischer, J. T. O'Bryan, R. Lopez, and H. P. Stahl, "Vector formulation for interferogram surface fitting," *Applied Optics* **32** (25), 4738-43, 1993.

24. K. A. Goldberg, P. Naulleau, S. Lee, C. Bresloff, D. Attwood, J. Bokor, "High-accuracy interferometry of EUV lithographic optical systems," Journal of Vacuum Science & Technology B **16** (6), 3435-3439, 1998.

25. K. A. Goldberg, "EUV Interferometry," doctoral dissertation, Department of Physics, University of California, Berkeley, 261, 1997.